

Supporting Information

High-Quality Perovskite Quantum Dots with Excellent Reproducibility and Amplified Spontaneous Emission by Optimization of Cesium Precursor

Liang Tao^{1,2, †}, Chenghao Bi^{1,2,3, †*}, Xingyu Wang^{4,5}, Shibo Wei^{1,2}, Ke Ren^{1,2}, Xuexuan Huang^{1,2}, Chiyu Guo^{1,2}, Jiang Hu^{1,2}, Nora H. de Leeuw^{4,5}, Wenxin Wang^{1,2, *}

¹ Qingdao Innovation and Development Base, Harbin Engineering University, Qingdao 266000, China.

² College of Physics and Optoelectronic Engineering, Harbin Engineering University, Harbin 150001, China.

³ Yantai Research Institute, Harbin Engineering University, Yantai 264000, China.

⁴ School of Chemistry, University of Leeds, Leeds LS2 9JT, UK.

⁵ Department of Earth Sciences, Utrecht University, 3584 CB Utrecht, The Netherlands.

Corresponding author:

*chenghao.bi@hrbeu.edu.cn

*wenxin.wang@hrbeu.edu.cn

Experimental Section

Materials: Chemicals and Reagents: Cesium carbonate (Cs_2CO_3 , Aladdin, 99.9%), Cesium acetate (CsOAc , Aladdin, 99.9%), lead bromide (PbBr_2 , Youxuan, 99.9%), oleic acid (OA, Alfa-Aesar, 90%), 2-hexyldecanoic acid (2-HA, TCI, >98%), oleylamine (OAm, Aladdin, 90%), octadecene (ODE, Sigma-Aldrich, 90%), n-hexane (Aladdin, 98%), methyl acetate (Aladdin, 99%). All these reagents are used without further purification.

Preparation of Cs_2CO_3 -OA Precursor: The precursor for synthesizing CsPbBr_3 quantum dots (QDs) is the cesium oleate (CsOL), prepared by loading into 250 mL of three-neck flask from 10 mL of ODE and 100 mg Cs_2CO_3 , and the mixture is degassed under stirring and is slowly heated to 100 °C for 1 hour at vacuum conditions. Subsequently, with the flow of nitrogen (N_2), the reaction mixture adds in 0.7 mL of dried OA to remove the oxygen and water, heats at 100 °C until complete dissolution of Cs_2CO_3 . The mixture of CsOL is cooled to room temperature for injection and is stored under an inert atmosphere.

Preparation of CsOAc-OA Precursor: The precursor for synthesizing CsPbBr_3 QDs is the CsOL, prepared by loading into 250 mL of three-neck flask from 10 mL of ODE and 117.8 mg CsOAc, and the mixture is degassed under stirring and is slowly heated to 100 °C for 1 hour at vacuum conditions. Subsequently, with the flow of nitrogen (N_2), the reaction mixture adds in 0.7 mL of dried OA to remove the oxygen and water, heats at 100 °C until complete dissolution of CsOAc. The mixture of CsOL is cooled to room temperature for injection and is stored under an inert atmosphere.

Preparation of CsOAc-2-HA Precursor: The precursor for synthesizing CsPbBr_3 QDs is prepared by loading into 250 mL of three-neck flask from 10 mL of ODE and 117.8 mg CsOAc, and the mixture is degassed under stirring and is slowly heated to 100 °C for 1 hour at vacuum conditions. Subsequently, with the flow of nitrogen (N_2), the reaction mixture adds in of 0.7 mL of dried 2-HA to remove the oxygen and water, heats at 100 °C until complete dissolution of CsOAc. The mixture

of cesium source is cooled to room temperature for injection and is stored under an inert atmosphere.

Synthesis of CsPbBr₃ QDs: 138 mg of lead bromide (PbBr₂) is added into a 250 mL of three-necked flask along with 10 mL of ODE, and the mixture is injected under N₂ at 120 °C for 30 min with continuously stirring. In this process, the cycle of vacuum and N₂ purging is repeated three times to remove the oxygen and water. Subsequently, 1 mL dried OA and 1 mL dried OAm are injected into the mixture under N₂. Then, we swiftly inject into the solution with 0.8 mL of CsOL (pre-heated at 40 °C or 100 °C), upon the reaction temperature is elevated to 180 °C. After 5 s, the reaction is terminated quickly by the ice-water bath. The crude QDs is precipitated by adding methyl acetate and is centrifuged at 8500 rpm for 5 min to remove the unreacted ligands and excess precursors. Then, the precipitate is dissolved in hexane for subsequent measurement of optical properties.

Characterization of CsPbBr₃ QDs: Steady-state ultraviolet-visible (UV-vis) absorption is measured utilizing a Perkin Elmer Lambda 1050+ UV spectrophotometer. Steady-state PL emission is acquired by an F-380 spectrometer. An Oxford Instruments Optistat-DN is measured temperature-dependent PL spectra in the range 80-220 K. Transmission electron microscopy (TEM) images are acquired on a JEM-2100 (JEOL) operated at 200 kV. X-ray diffraction (XRD) is performed using Cu K α radiation ($\lambda = 1.5418 \text{ \AA}$) on an X-ray diffractometer (Bruker, D8 Focus). The time-resolved photoluminescence decay spectra of QDs are acquired by coupling a Horiba Fluorolog spectrophotometer with a 375 nm, 45 ps pulsed laser and a time-corrected single-photon counting system. The photoluminescence quantum yields (PLQY) is obtained using an integrating sphere (Edinburgh, FLS920) with an excitation wavelength of 530 nm. The time-resolved PL decays (TRPL) of QDs is obtained using a Horiba Fluor log spectrometer with a 375 nm, 45 ps pulsed laser and a time-corrected single photon counting system. X-ray photoelectron spectroscopy (XPS) is recorded on a PHI 5000 Versa Probe III spectrometer using a monochromatic AlK α radiation source (1486.6 eV). The TA of the sample is measured using a 1030 nm femtosecond laser as the

probing light source, which is generated through an optical parametric amplifier (OPA) to obtain a 420 nm excitation light, through Ultrafast Transient Absorption Spectrometer (TIME-TECH SPECTRA, TA-ONE-1).

The ASE Measurements: A femtosecond laser system (420 nm, 40 fs, 66.7 $\mu\text{J}\cdot\text{pulse}^{-1}$, 150 kHz repetition rate) is used as the laser source, and femtosecond pump-probe TA is used for measurement.

First-Principles Calculations: All calculations based on Density Functional Theory (DFT) are performed with the Perdew-Burke-Ernzerhof (PBE) density functional using the generalized gradient approximation (GGA) in the Vienna Ab initio Simulation Package (VASP). Geometry optimizations is carried out for ion-electron interactions using the Projection Augmented Wave (PAW) method. All atomic positions and lattice constants are fully relaxed until the atomic forces is less than 0.02 eV/Å. The total energies of all structures are converged to 10^{-5} eV. A plane-wave cutoff energy of 400 eV is used for the expansion. Electronic structure calculations are performed using an $8\times 8\times 1$ Monkhorst-Pack k -point mesh sampling.

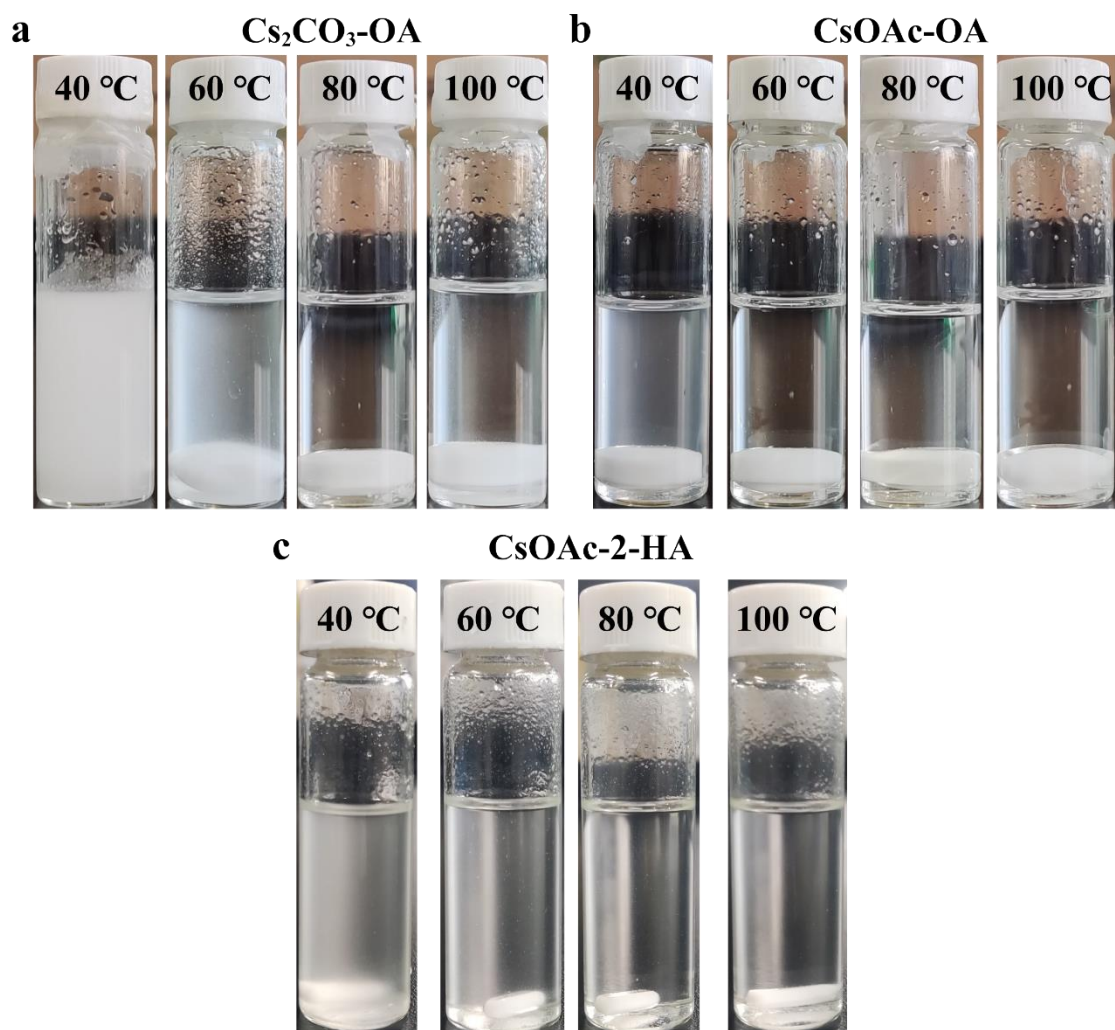


Figure S1. CsOL made by Cs_2CO_3 or CsOAc mixing with OA or 2-HA at different temperature. From left to right are the physical images of **(a)** the CsOL precursor obtained from mixing Cs_2CO_3 with OA and ODE at 40 °C, 60 °C, 80 °C, 100 °C, and **(b)** the CsOL precursor obtained from CsOAc with OA and ODE at 40 °C, 60 °C, 80 °C, 100 °C, and **(c)** the CsOL precursor obtained from CsOAc with 2-HA and ODE at 40 °C, 60 °C, 80 °C, 100 °C, respectively.

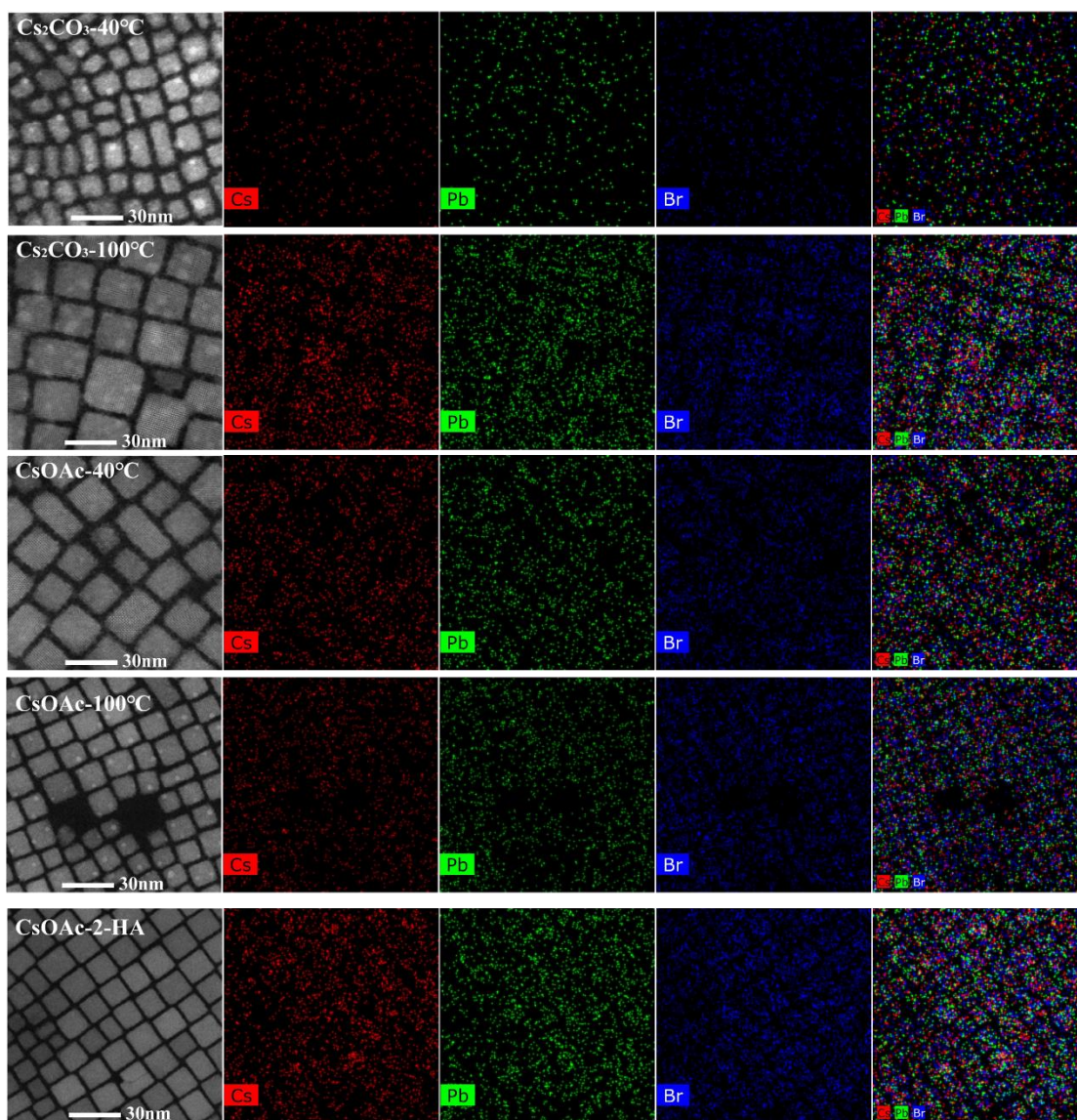


Figure S2. EDS profiles of the Cs_2CO_3 -40 °C, Cs_2CO_3 -100 °C, CsOAc -40 °C, and CsOAc -100 °C quantum dots (QDs).

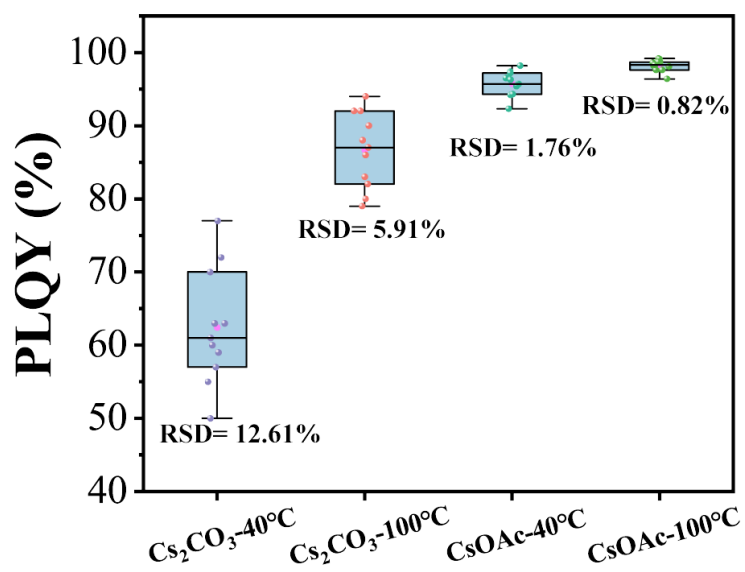


Figure S3. The error bar plot for of PLQY for Cs₂CO₃-40 °C, Cs₂CO₃-100 °C, CsOAc-40 °C, and CsOAc-100 °C QDs.

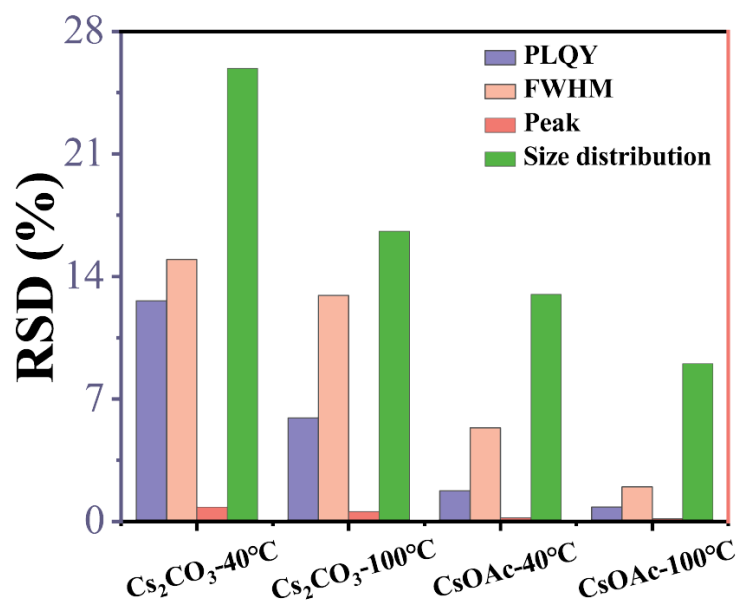


Figure S4. The RSD plot for of PLQY, FWHM, peak position and size distribution for Cs₂CO₃-40 °C, Cs₂CO₃-100 °C, CsOAc-40 °C, and CsOAc-100 °C QDs.

We prepared some different CsOL precursors made by mixing Cs₂CO₃ or CsOAc with OA and ODE to synthesize the QDs at 40 °C and 100 °C, and measured the TEM, PL spectra, and PLQY to analyze the RSD (relative standard deviation) of morphology and optical properties, as shown in **Supplement Fig. S4**. In the RSD of morphology and optical characteristics, the smaller the RSD is, the more excellent reproducibility of QDs is. The RSD plot for of PLQY, FWHM, PL emission peak wavelength and size distribution for these QDs showed that the RSD of CsOAc-40 °C, CsOAc-100 °C QDs was obvious smaller than that of Cs₂CO₃-40 °C and Cs₂CO₃-100 °C QDs, which further proved that AcO⁻ could optimize the nucleation and growth process of QDs and improve the reproducibility of QDs by accelerating the complete conversion degree of cesium salt.

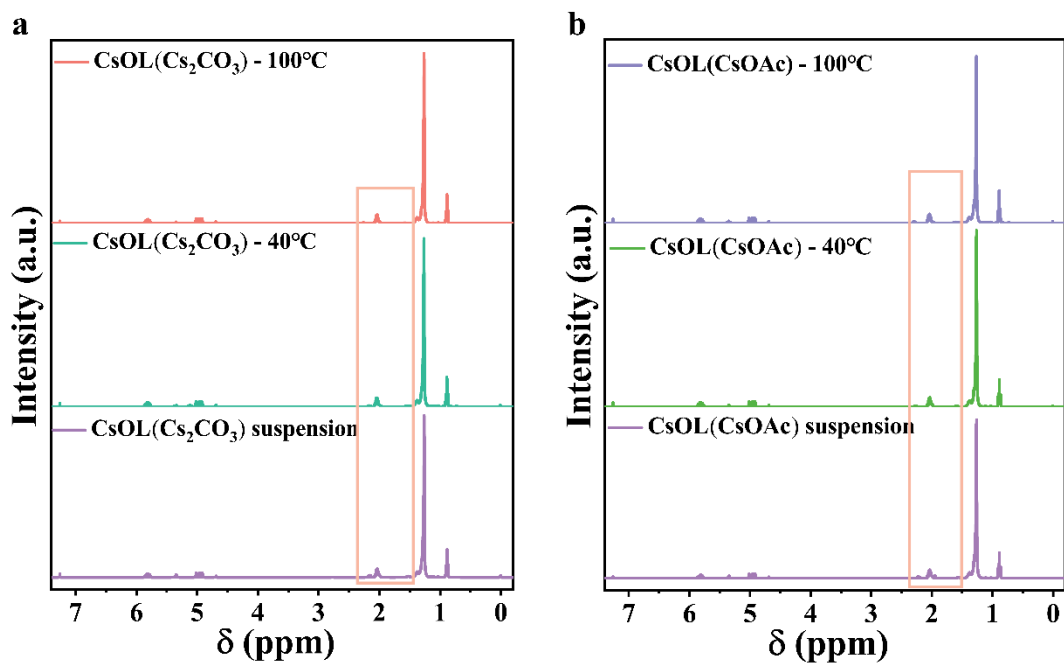


Figure S5. Full ¹H NMR spectra for (a) CsOL (Cs₂CO₃) supernatant at 40 °C, CsOL (Cs₂CO₃) supernatant at 100 °C and CsOL (Cs₂CO₃) supernatant in the case of excess cesium carbonate saturation, and (b) CsOL (CsOAc) supernatant at 40 °C, CsOL (CsOAc) supernatant at 100 °C and CsOL (CsOAc) supernatant in the case of excess cesium acetate saturation.

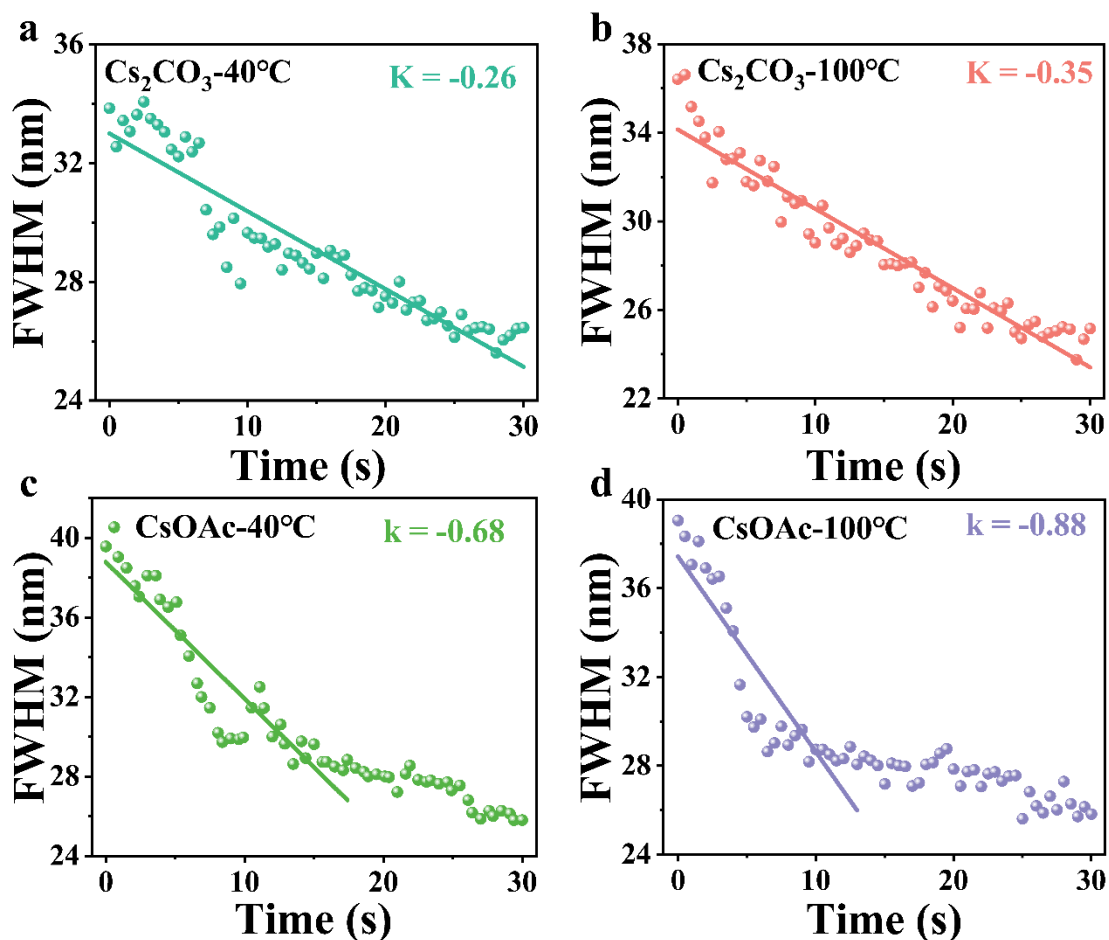


Figure S6. The relationship between the FWHM of the *in-situ* PL spectra and time for (a) Cs_2CO_3 -40 °C, (b) Cs_2CO_3 -100 °C, (c) CsOAc -40 °C, and (d) CsOAc -100 °C QDs.

The slope between the time of the nucleation and growth process and the QDs synthesized in the way, is shown in **Supplement Fig. S6**. It reflected the speed of nucleation and growth process. When we injected the cesium precursor into lead precursor, the CsPbBr_3 QDs immediately generated. But this size of QDs was irregular and uneven, which would rectify the size and remove the defect of the QDs with the aid of organic ligand in the cooling process. It looked like the “annealing” process, and it leads to the decreasing of the FWHM. Therefore, the slope in the evolution of FWHM and the time of growth of the QDs prepared by AcO^- , was quite larger and shorter than that of by Cs_2CO_3 , which further verified the effect of AcO^- to expedite the nucleation and growth process of QDs.

To further study the role of AcO^- , we have utilized the CsOL precursor made by mixing Cs_2CO_3 with HOAc and ODE as cesium resource in the process of synthesizing QDs (HOAc- Cs_2CO_3 QDs), and have utilized the CsOL precursor made by mixing Cs_2CO_3 with HOAc, OA and ODE as cesium resource in the process of synthesizing QDs (HOAc- Cs_2CO_3 -OA QDs).

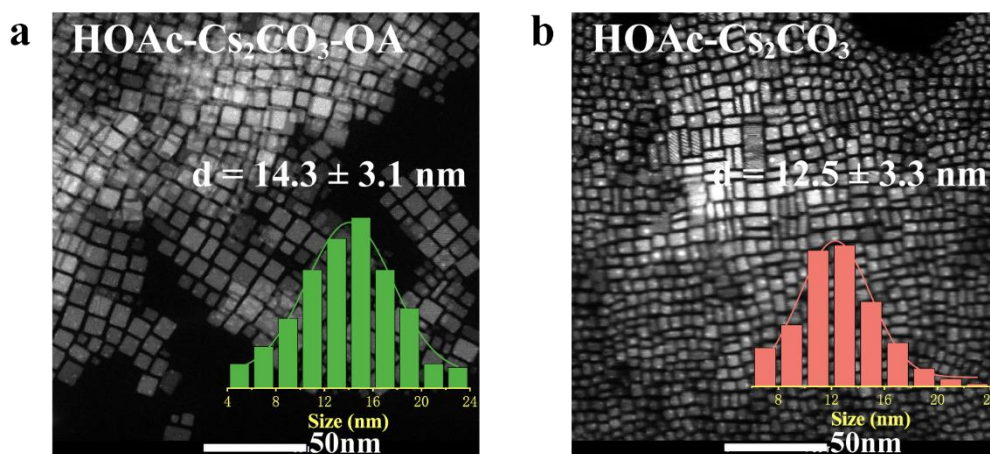


Figure S7. TEM images of (a) HOAc- Cs_2CO_3 -OA, and (b) HOAc- Cs_2CO_3 QDs. Inserts show the corresponding size distribution histograms.

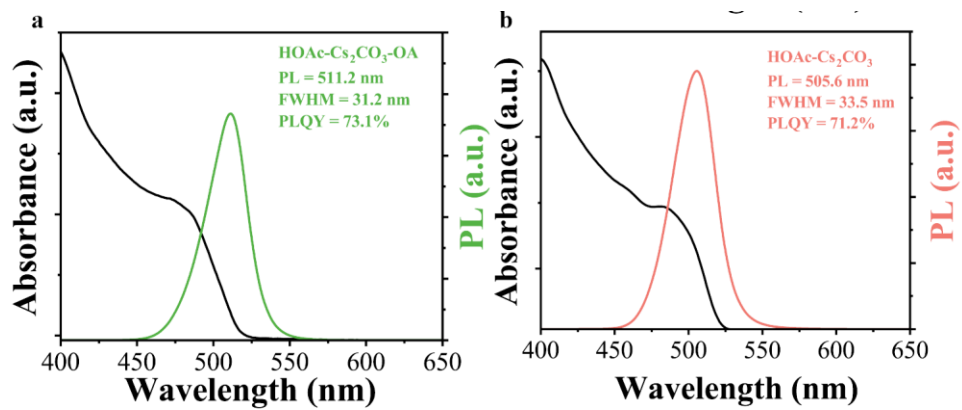


Figure S8. UV-vis absorption and PL spectra of (a) HOAc-Cs₂CO₃-OA, and (b) HOAc-Cs₂CO₃ QDs.

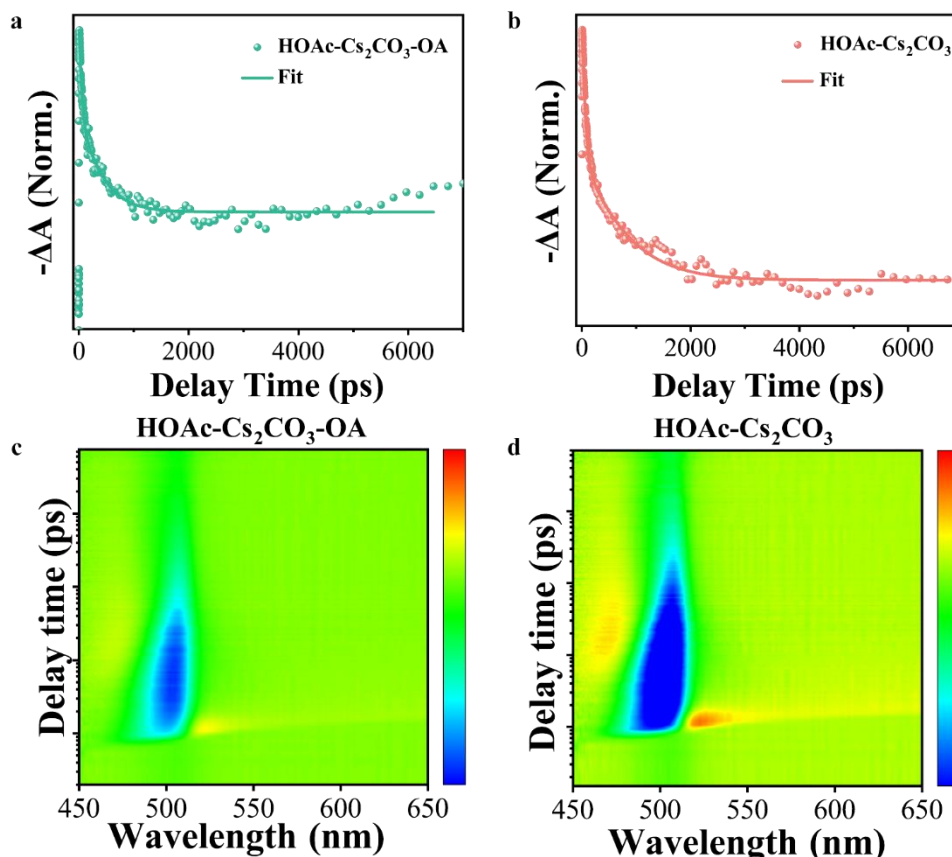


Figure S9. The pseudo color image of TA and TA bleach dynamics curves of (a), (c) HOAc-Cs₂CO₃-OA, and (b), (d) HOAc-Cs₂CO₃ QDs.

To further verify our viewpoint, we have measured the femtosecond transient absorption (TA) spectra, as shown in **Supplement Fig. S9**, with fitting parameters elucidated in **Supplement Table S2**. HOAc-Cs₂CO₃ and HOAc-Cs₂CO₃-OA QDs exhibited the shorter slow component and fast component comparing with Cs₂CO₃-OA QDs, indicating the higher defects density of these QDs. Meanwhile, the HOAc-Cs₂CO₃ and HOAc-Cs₂CO₃-OA QDs manifested short excited state lifetime of 557.79 ps and 303 ps, which was one order of magnitude lower than that of the other QDs. Combining with TEM images, PL and UV spectra and TA spectra of the HOAc-Cs₂CO₃ and HOAc-Cs₂CO₃-OA QDs in **Supplement Fig. S7-9**, we think HOAc as surface ligand are severe uniform size distribution, serious optical properties.

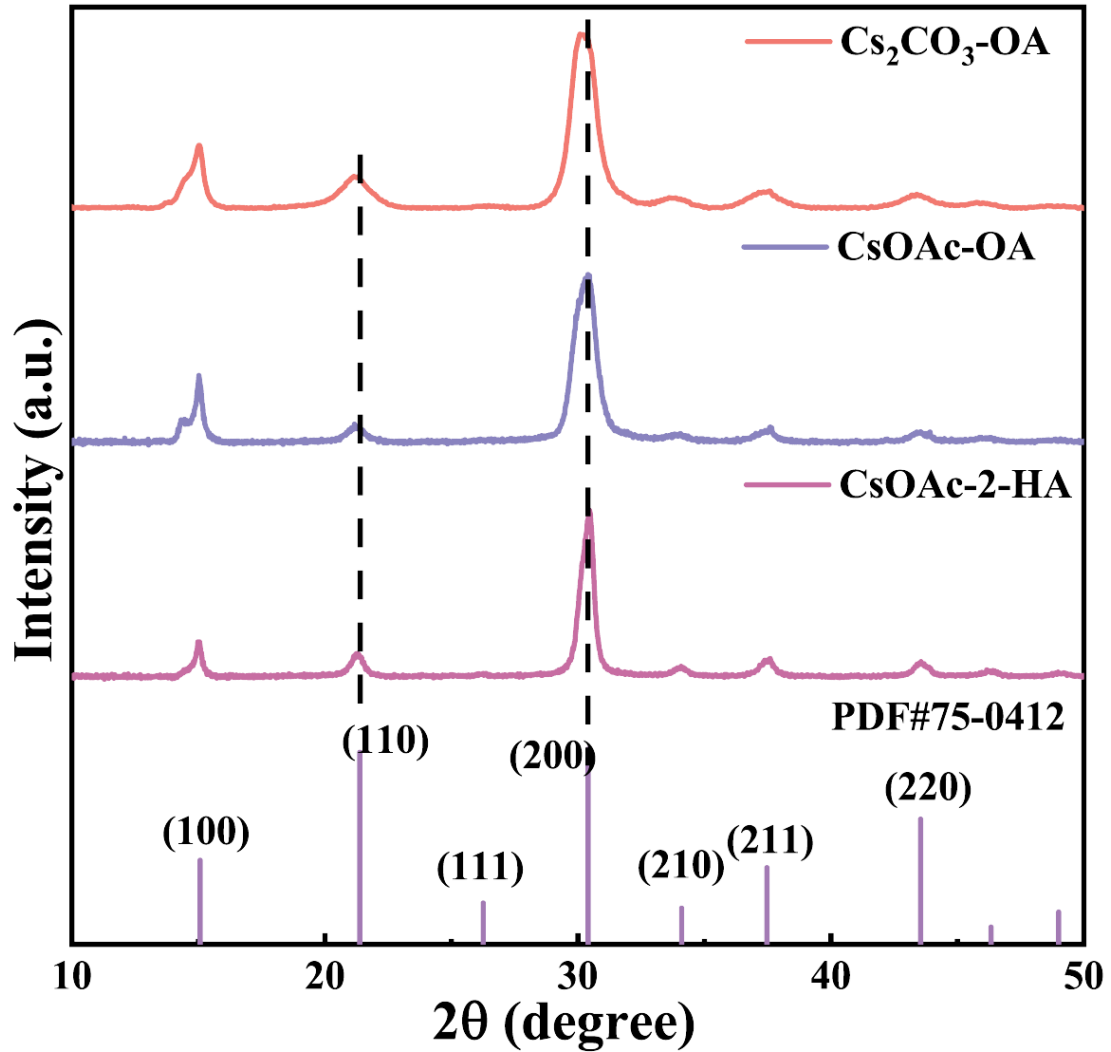


Figure S10. Comparison of XRD pattern of the $\text{Cs}_2\text{CO}_3\text{-OA}$, CsOAc-OA and CsOAc-2-HA QDs with PDF standard card.

The X-ray diffraction (XRD) pattern investigates the crystalline structure of CsPbBr_3 , as depicted in **Supplement Fig. S10**. The XRD pattern of CsOAc-OA and CsOAc-2-HA QDs could be indexed as orthorhombic CsPbBr_3 (PDF #75-0412), but the (200) diffraction peak at $\text{Cs}_2\text{CO}_3\text{-OA}$ QDs shifted to a lower angle. It indicated that the structure of $\text{Cs}_2\text{CO}_3\text{-OA}$ QDs was not stable to sustain the orthorhombic system.

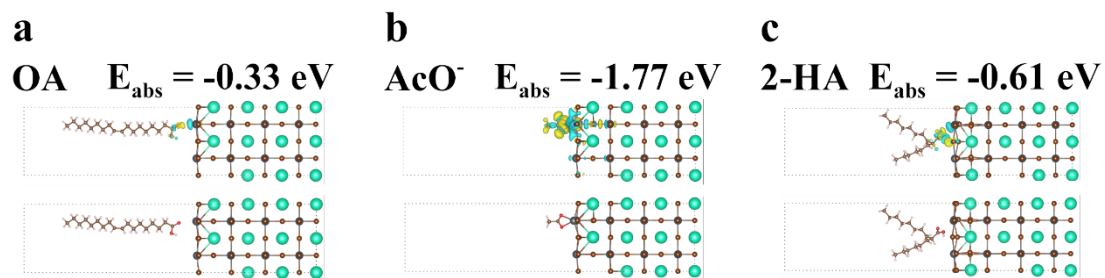


Figure S11. DFT simulation results of the binding energies of (a) Cs₂CO₃-OA, (b) CsOAc-OA, (c) CsOAc-2-HA QDs surface.

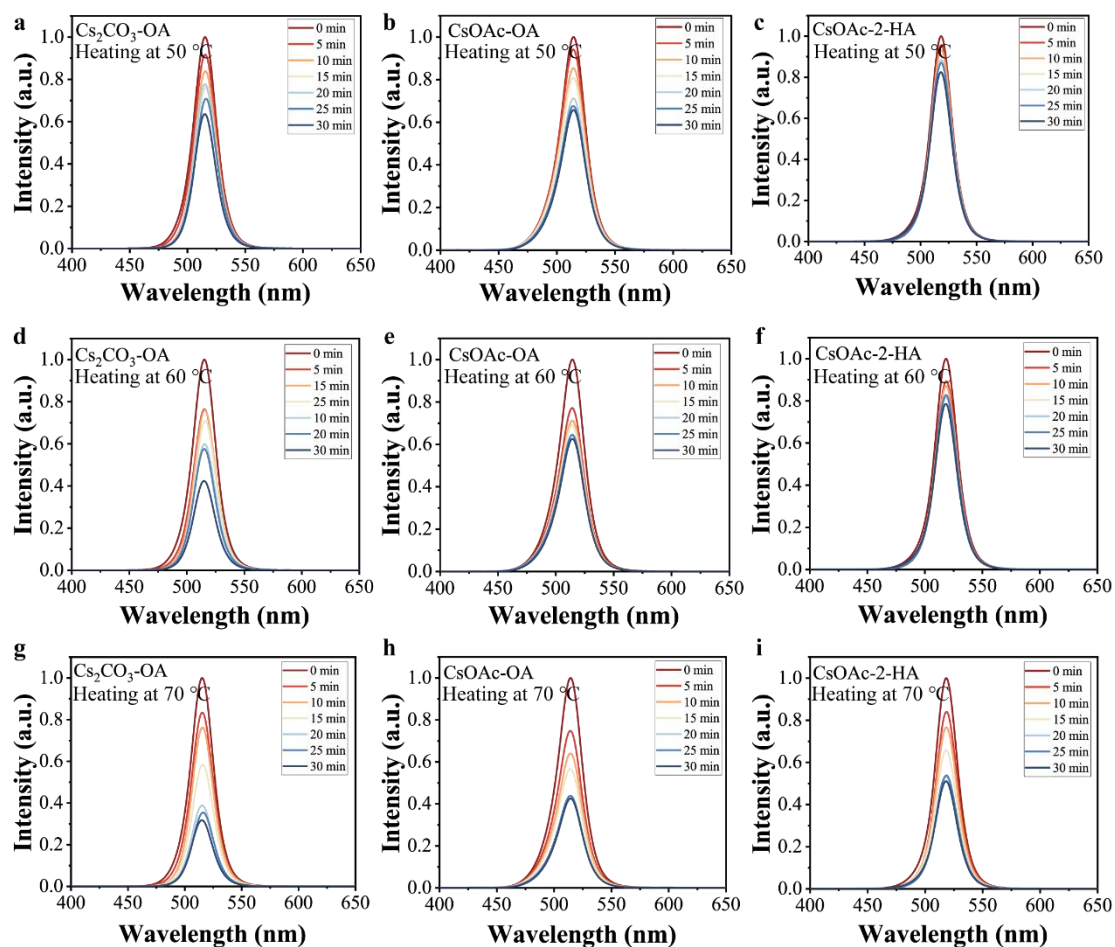


Figure S12. Thermal stability of (a), (d), (g) $\text{Cs}_2\text{CO}_3\text{-OA}$, (b), (e), (h) CsOAc-OA , and (c), (f), (i) CsOAc-2-HA QDs under continuous heating treatment at 50 °C, 60 °C and 70 °C for 30 min, respectively.

The thermal stability of the $\text{Cs}_2\text{CO}_3\text{-OA}$, CsOAc-OA , and CsOAc-2-HA QDs was measured to analyze the relationship between the high temperature and the stability of optical properties of these QDs, as illustrated in **Supplement Fig. S12**. It was observed that the PL intensity of $\text{Cs}_2\text{CO}_3\text{-OA}$ QDs has shown rapid attenuation at intervals, even less than half of the original after half an hour. On the contrary, the CsOAc-OA and CsOAc-2-HA QDs demonstrated excellent thermal stability of PL intensity, especially CsOAc-2-HA QDs only displayed a 20% decay after half an hour. Furthermore, we measure the PL under continuous heating at different temperatures. It is observed that the PL intensity of CsOAc-2-HA QDs attenuate slightly after heating 30 min at 50 °C, and the PL intensity of $\text{Cs}_2\text{CO}_3\text{-OA}$ QDs drop dramatically, which is less than half of initial value after heating 30 min. And CsOAc-2-HA QDs (less than 50% decay) also

exhibit a better thermal stability than that of $\text{Cs}_2\text{CO}_3\text{-OA}$ QDs (over 70% decay) after half an hour under continuous heating at 70 °C. As a result, the CsOAc-2-HA QDs the excellent thermal stability of PL intensity under continuous heating at different temperatures.

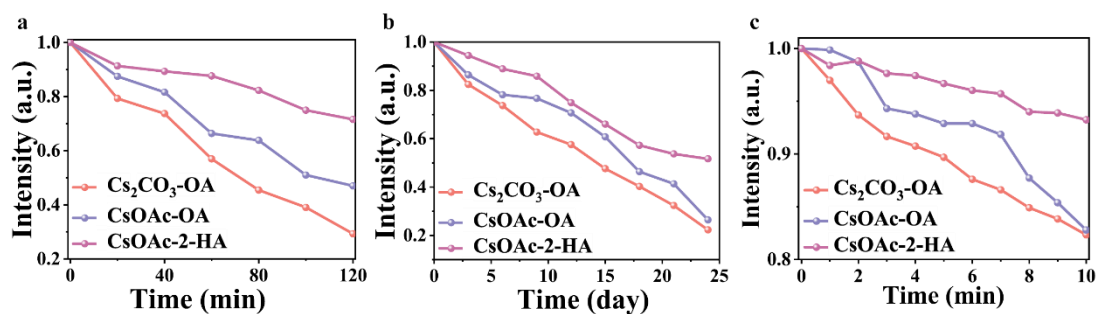


Figure S13. Stability verification of PL spectra of $\text{Cs}_2\text{CO}_3\text{-OA}$, CsOAc-OA , CsOAc-2-HA QDs under (a) prolonged UV irradiation, (b) prolonged storage in room temperature environment, and (c) prolonged pumped emission.

To prove the stability effect of 2-HA and AcO^- , QDs was treated the PL intensity dependency on time under prolonged UV irradiation, prolonged storage in room temperature environment, and prolonged pumped emission in **Supplement Fig. S13**. It became apparent that a faster rate of decreasing in CsOAc-2-HA QDs, which demonstrated that CsOAc-OA QDs could efficiently overcome the issue of degradation and spectral stability in some different environment.

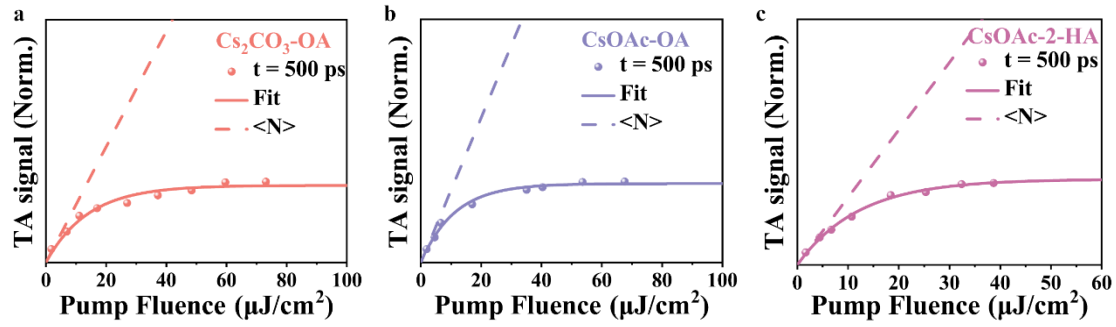


Figure S14. Normalized an exciton bleach signal at a delay time of 500 ps measured as a function of the excitation densities and its fitting to a Poisson statistics model for the (a) Cs₂CO₃-OA, (b) CsOAc-OA, (c) CsOAc-2-HA QDs. Dashed line is the average exciton occupancy $\langle N \rangle$ at each excitation density.

The dynamical features of exciton bleaching are probed under varying pump intensity, revealing the emergence of rapid decay components during several hundred picoseconds. These decay components exhibit a non-linear arising and fast decay components appear on the time scale of a few to tens of ps with increasing pump intensity, characteristic of typical multiexciton recombination phenomena. Several biexciton lifetimes of QDs are collected from the TA kinetics of varying pump intensity as the function of excitation densities, then a time point of 500 ps is selected randomly and is subjected to normalization. By fitting the amplitude saturation curve of the biexciton lifetime dependency on excitation density to the exponential equation: $I = 1 - e^{-CP}$, where C is a fitting parameter proportional to the absorption cross-section of the QDs. And the average exciton occupancy for each QDs ($\langle N \rangle = CP$) is derived, as illustrated in **Supplement Fig. S14**. Subsequently, the dynamics of biexciton recombination is calculated by a specific subtraction of the dynamics and normalization, where $\langle N \rangle$ is much smaller than 1, since in this case the kinetic difference is mainly contributed by a fraction (low percentage) of biexcitons in the QDs, while the high-order multiple excitons in QDs can be neglected. And we can get the normalization curve¹⁻³.

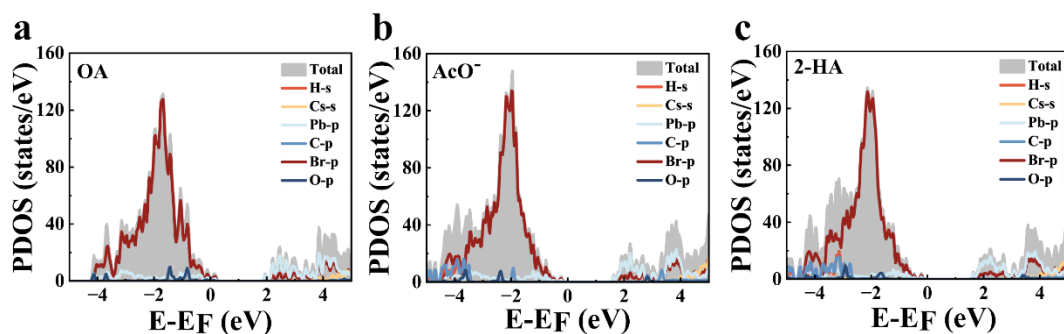


Figure S15. Differential charge density distributions of (a) $\text{Cs}_2\text{CO}_3\text{-OA}$, (b) CsOAc-OA , (c) CsOAc-2-HA QDs interactions.

To further investigate the mechanism of AcO^- and 2-HA ligands modification on QDs, first-principles calculations based on Density Functional Theory (DFT) were employed to analyze and elucidate the intricate electronic interplay and density of states between QDs surfaces and the OA, AcO^- , and 2-HA. Considering that the ligand interface with CsPbBr_3 involves the CsBr and PbBr_2 crystal faces, structural relaxation occurred at the PbBr_2 interface of CsPbBr_3 rather than the CsBr interface. Therefore, heterojunctions are carried out by adsorbing OA or 2-HA ligands onto the PbBr_2 crystal interface of the CsPbBr_3 (001) surface. To probe the structural stability of the combination between different ligands and the QDs surfaces, the absorption energy was calculated and illustrated in **Supplement Fig. S11**. The charge transfer between ligands and QDs showed in the blue and yellow regions, reflected the strength of the interaction, where blue region denotes charge depletion and yellow region denotes charge accumulation. The region of charge transfer from two short branched-chain ligand 2-HA was larger than that OA. It indicated 2-HA and AcO^- are beneficial to the transport and recombination of charge carriers. In the density of states plots of $\text{Cs}_2\text{CO}_3\text{-OA}$ QDs, the appearance of mid-gap states near 0 eV was attributed to defects in CsPbBr_3 , leading to trap states within the bandgap, as depicted in **Supplement Fig. S15**. Notably, when AcO^- or 2-HA was used, the mid-gap states vanished, with charge accumulation concentrated near the surface of the QDs and within its interior. The absorption energy of 2-HA (-0.61 eV) and AcO^- (-1.77 eV) was found to be lower than that of oleic acid (-0.33 eV). It indicated stronger interactions between CsPbBr_3 QDs and 2-HA and AcO^- compared to OA. Since QDs is composed of Cs, Pb, and Br elements, while C, H, and

O elements constitute the organic ligands, the overlap between Cs, Pb, and Br orbitals and C, H, and O orbitals implies potential orbital hybridization and energy overlap between the ligands and QDs. In contrast with this, the absence of overlap indicated that these properties at the band edge are solely determined by either the QDs or the ligands. In the energy range of -5 eV to -3 eV, the overlap of the density of states between AcO^- and 2-HA and QDs increased, indicating a stronger interaction between AcO^- , 2-HA and QDs than OA. Moreover, these overlap regions between ligands and QDs lie within the bandgap. It suggested that these ligands do not directly influence the optical properties of QDs, but rather affected the optical properties after surface modification. Combining with the region of charge transfer, the AcO^- and 2-HA effectively store electrons and reduce the build-up of charge in QDs, which could reduce exciton binding energy. Consequently, the theoretical results validate this obtained from experimental testing, which the AcO^- and 2-HA can effectively optimize the surface defects of QDs and enhancing their luminescence performance.

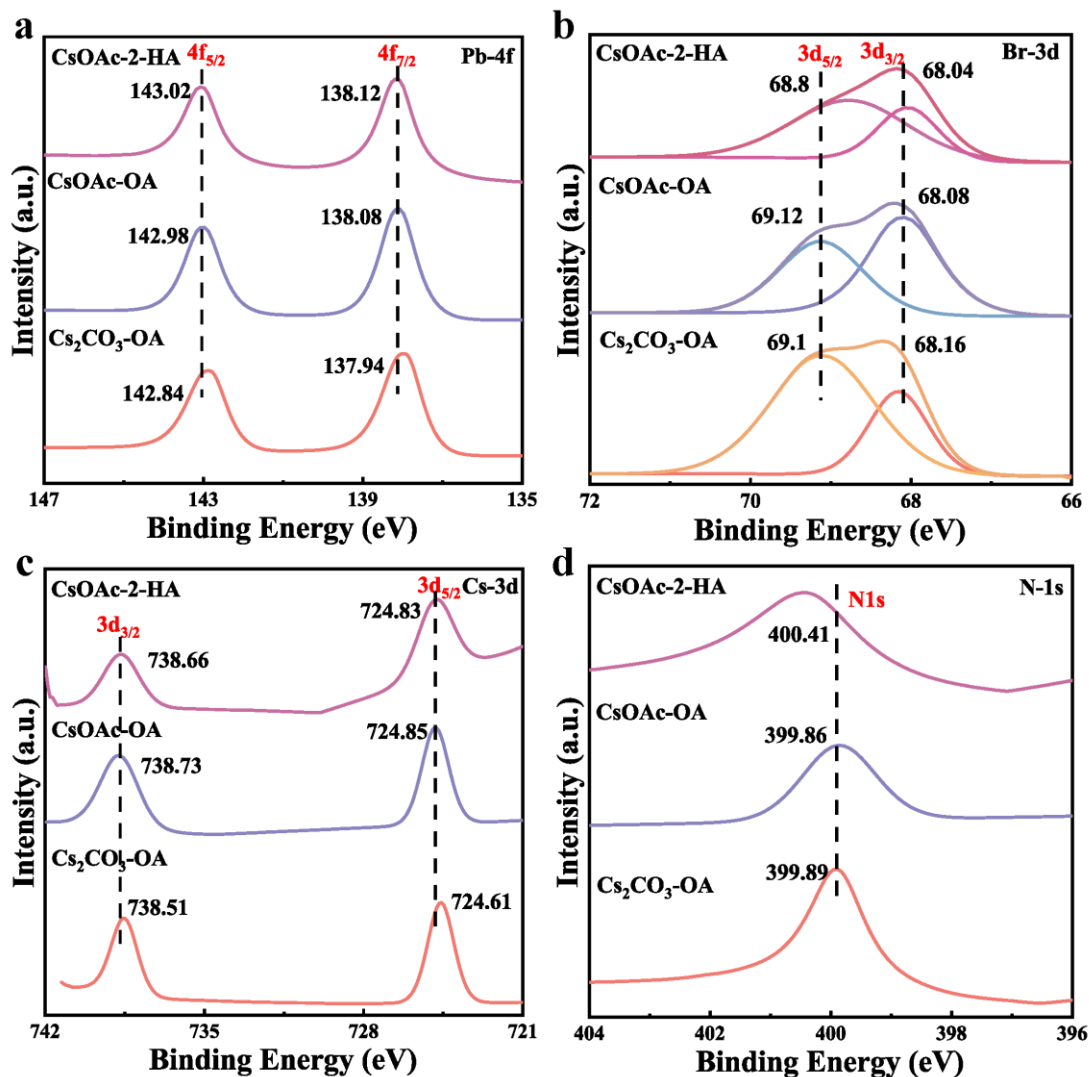


Figure S16. XPS survey spectrum of Cs₂CO₃-OA, CsOAc-OA and CsOAc-2-HA QDs. (a) Pb-4f spectrum, (b) Br-3d spectrum, (c) Cs-3d spectrum, (d) N-3s spectrum. All peaks are calibrated using C 1s (284.8 eV).

X-ray photoelectron spectroscopy (XPS) spectra is measured to analyze binding energy, as illustrated in **Supplement Fig. S16**. The Pb-4f levels observed at 143.02 eV and 138.12 eV (CsOAc-2-HA QDs) were both shifted to a higher binding energy by 0.18 eV, and that observed at 142.98 eV and 138.08 eV (CsOAc-OA QDs) are both shifted to a higher binding energy by 0.14 eV, compared to the Cs₂CO₃-OA QDs of 142.84 eV and 137.94 eV. Meanwhile, the Cs-3d levels observed at 738.66 eV and 724.84 eV (CsOAc-2-HA QDs) are both shifted to a higher binding energy by 0.15 eV and 0.22 eV, and that observed at 738.73 eV and 724.85 eV (CsOAc-OA QDs) are both shifted to a higher binding energy by 0.22 eV and 0.24 eV, compared to the Cs₂CO₃-

OA QDs of 738.51 eV and 724.61 eV. It was attributed to the more powerful interaction between Pb^{2+} and AcO^- or 2-HA than Pb^{2+} and OA.

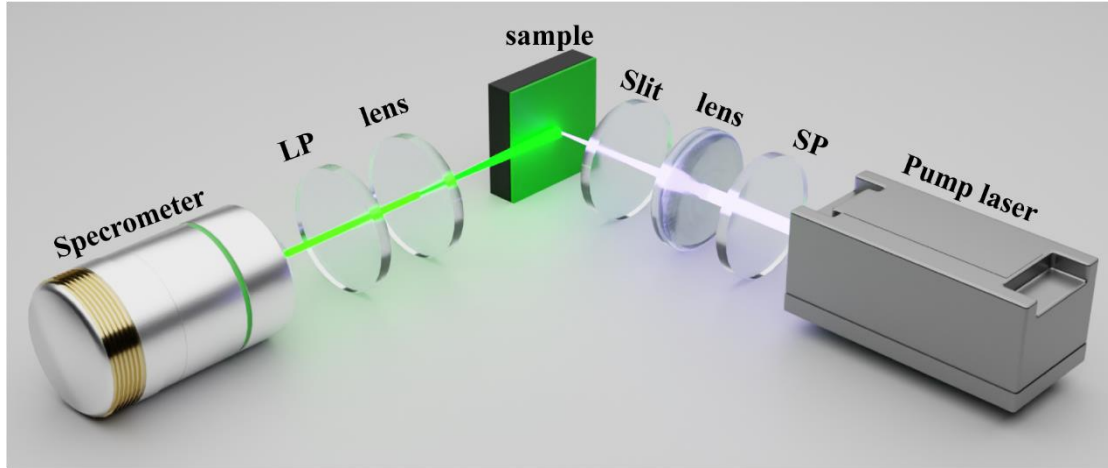


Figure S17. The optical setup for ASE measurement of CsPbBr₃ QDs

We have measured the ASE Performance of CsPbBr₃ QDs, and the optical setup is presented in **Supplement Fig. S17**. A 420 nm femtosecond laser beam is lasing from an optical parametric amplification (40 fs, 66.7 μ J/pulse, 150 kHz repetition rate). A short-pass filter is placed to leach out the rest idle light. Then, the pump light is shot on the surface of CsPbBr₃ QDs through a focusing lens, and the emission light is collected by spectrometer through a focusing lens, long-pass filter, and objective lens in sequence.

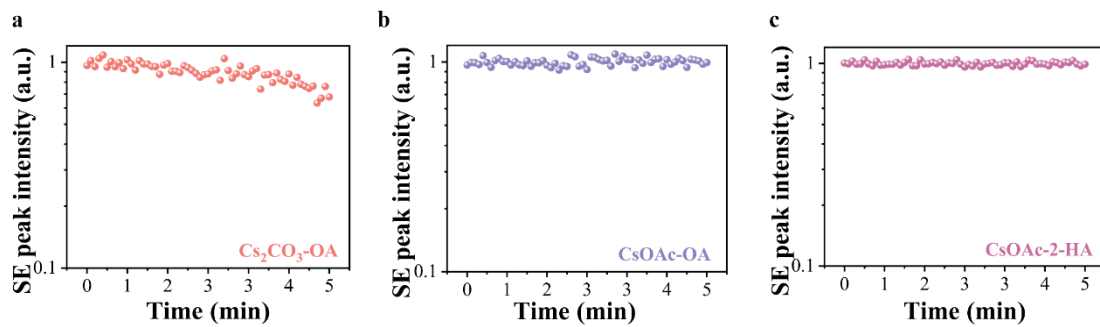


Figure S18. Photostability of ASE intensity of (a) $\text{Cs}_2\text{CO}_3\text{-OA}$, (b) CsOAc-OA , and (c) CsOAc-2-HA QDs under $1.2P_{\text{th}}$ pump fluence.

The photostability of ASE intensity of QDs are measured, as illustrated in **Supplement Fig. S18**. The ASE intensity of the CsOAc-2-HA QDs almost unchanged under the intensity during 5 min. While the ASE intensity of the CsOAc-OA QDs have slight fluctuations under the same measure condition. However, the ASE intensity of the $\text{Cs}_2\text{CO}_3\text{-OA}$ QDs exhibit apparent decrease. Therefore, we think that CsOAc-2-HA QDs show the best ASE photostability than that of the other QDs.

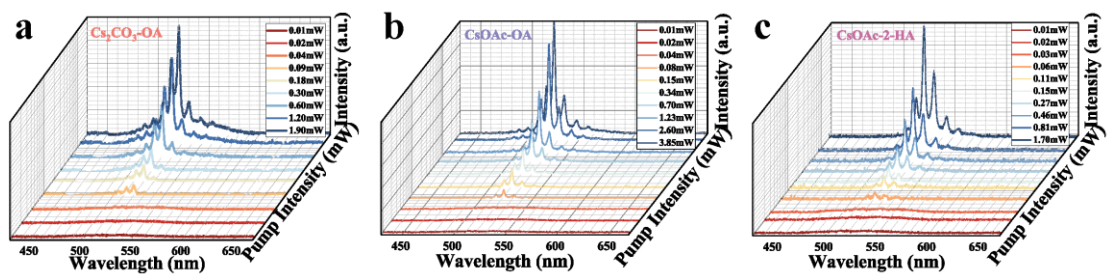


Figure S19. The pump density-dependent emission spectra of (a) $\text{Cs}_2\text{CO}_3\text{-OA}$, (b) CsOAc-OA , and (c) CsOAc-OA QDs .

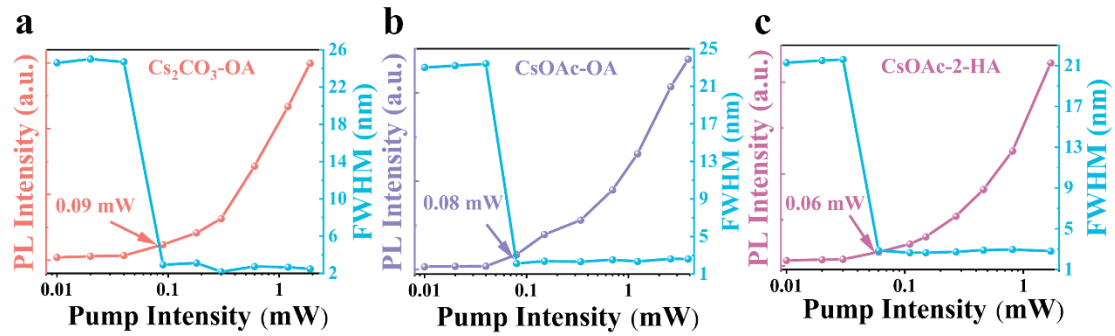


Figure S20. The dependence of the output intensity and FWHM as a function of pump density of (a) Cs₂CO₃-OA, (b) CsOAc-OA, and (c) CsOAc-2-HA QDs.

Perovskite QDs is sandwiched by two DBR mirrors as a surface emitting random lasers to investigate the laser performance, which shows the great advantage to CsOAc-2-HA QDs, as depicted in **Supplement Fig. S19, 20**. With the increasing pump laser fluence, the broad emission peaks gradually transitioned to several sharp emission peaks. And the FWHM of the emission spectrum presented a sharp reduction, accompanied by a swift increase in the emission intensity. When the pump laser fluence exceeded the threshold, the FWHM of Cs₂CO₃-OA, CsOAc-OA, and CsOAc-2-HA QDs rapidly decreased to 2.2 nm, 2.3 nm and 2.6 nm, respectively. A similar trend was observed for the emission intensity as a nonlinear process. And the emission intensity and FWHM of Cs₂CO₃-OA, CsOAc-OA, and CsOAc-2-HA QDs as a function of pumping laser fluence demonstrate the lasing action with a threshold of 1.55 $\mu\text{J}\cdot\text{cm}^{-2}$, 1.37 $\mu\text{J}\cdot\text{cm}^{-2}$ and 1.03 $\mu\text{J}\cdot\text{cm}^{-2}$, respectively. With these above excellently low laser threshold, CsOAc-2-HA QDs had a great potential for laser.

Table S1. The concentrations of Cs for various CsOL precursor made by mixing Cs₂CO₃ and CsOAc with ODE, OA or 2-HA at different temperatures

Sample Code	Cs Concentration of the solution to be tested [ug/L]	Cs Concentration of the sample [ug/L]	Conversion Rate of Cs Concentration [%]
Cs ₂ CO ₃ -40 °C	315.23	788085.78	70.26
Cs ₂ CO ₃ -100 °C	448.67	1121680.26	100
CsOAc-40 °C	446.62	1116552.79	98.59
CsOAc-100 °C	452.99	1132479.71	100
CsOAc-2-HA-40 °C	445.84	1114612.32	98.51
CsOAc-2-HA-100 °C	452.51	1131287.50	100

We assume that the cesium source has completely dissolved at 100 °C, which means all the conversion rate of Cs concentration for Cs₂CO₃-100 °C, CsOAc-100 °C and CsOAc-2-HA-100 °C QDs are 100%. It was obvious that the concentrations of Cs for various CsOL precursor from Cs₂CO₃-100 °C, CsOAc-100 °C and CsOAc-40 °C QDs are similar, which meant the CsOL precursor made by mixing CsOAc with 2-HA and ODE is completely soluble, even at a lower temperature. Moreover, the ratio of Cs₂CO₃-40 °C QDs to Cs₂CO₃-100 °C QDs was 70.26%, which was much less than the ratio of CsOAc-40 °C QDs to CsOAc-100 °C QDs (98.59%). It is means that the AcO⁻ greatly accelerates the complete conversion degree of CsOL.

Table S2. Summary of TA spectra fitting parameters for Cs₂CO₃-40 °C, Cs₂CO₃-100 °C, CsOAc-40 °C, CsOAc-100 °C, and CsOAc-2-HA QDs

Sample Code	f_1 [%]	t_1 [ps]	f_2 [%]	t_2 [ps]	T_{ave} [ps]
Cs ₂ CO ₃ -40 °C	10.77	19.79	89.23	1388.31	1408.10
Cs ₂ CO ₃ -100 °C	9.62	22.21	90.38	1587.99	1610.21
CsOAc-40 °C	9.19	22.17	90.82	1769.63	1791.81
CsOAc-100 °C	5.31	13.28	94.69	2499.05	2512.33
CsOAc-2-HA	2.20	6.91	97.80	4631.66	4638.57
HOAc-Cs ₂ CO ₃ - OA	16.84	6.38	83.16	296.62	303.00
HOAc-Cs ₂ CO ₃	16.33	7.90	83.67	549.89	557.79

Table S3. Summary of time-resolved PL fitting parameters for Cs₂CO₃-40 °C, Cs₂CO₃-100 °C, CsOAc-40 °C, CsOAc-100 °C, and CsOAc-2-HA QDs.

Sample Code	f_1 [%]	t_1 [ns]	f_2 [%]	t_2 [ns]	T_{ave} [ns]	PLQY [%]	T_r [ns]	K_{nr} $\times 10^{-2}$ [ns ⁻¹]
Cs ₂ CO ₃ - 40 °C	8.90	9.73	91.10	10.08	19.81	62	12.28	3.09
Cs ₂ CO ₃ - 100 °C	58.74	17.76	41.26	4.41	22.17	87	19.29	0.67
CsOAc- 40 °C	69.51	26.22	30.49	2.89	29.12	93	27.08	0.26
CsOAc- 100 °C	100.00	33.99	/	/	33.99	95	32.29	0.16
CsOAc-2- HA	100.00	82.98	/	/	82.98	99	82.15	0.01

Table S4. FTIR band assignment for solution of CsOL, CsOL (Cs₂CO₃) precipitate, and CsOL (CsOAc) precipitate.

Wavenumbers(cm⁻¹)	Functional Groups	Mode	Possible Molecule
3072	O=C-OH	Stretch	CsHCO ₃
2920, 2851, 1461	C-H	Stretch	CsOL, CsOAc, OED, OA
1711	C=O	Stretch	CsOL, Cs ₂ CO ₃ , CsHCO ₃ , OA, CsOAc
1641, 1540, 1374	C-O	Stretch	CsOL, CsHCO ₃ , Cs ₂ CO ₃ , CsOAc, OA
1284	C-O	Stretch	CsOL, CsOAc, OA
900, 715	C-H	Bend	CsOL, OED, OA

Table S5. Summary of the ASE performance of perovskite.

Materials	Emission wavelength [nm]	Threshold [$\mu\text{J}\cdot\text{cm}^{-2}$]	Nano-structure	Ref.
PABr-CsPbBr ₃	524	25.45	films	4
MAPbBr ₃	545	3.07	films	5
CsPbBr ₃	519	9.45	QDs	6
CsPbBr ₃	515	240.5	films	7
CH ₃ NH ₃ PbBr ₃	533	140	films	8
CsPbBr ₃	520	120	QDs	9
CsPbBr ₃	520	17.6	QDs	10
CsPbBr ₃	515	22.25	films	11
CsPb(Br _{1-x} Cl _x) ₃	450-520	21	QDs	12
CsPbX ₃ (X=Cl, Br or I)	440-700	5	NC	13
CsPbBr ₃	515	0.54	QDs	This work

Reference

1. Li, Y. et al. Biexciton Auger recombination in mono-dispersed, quantum-confined CsPbBr₃ perovskite nanocrystals obeys universal volume-scaling. *Nano Research* **12**, 619-623 (2019).
2. Li, Y. et al. Size-and halide-dependent Auger recombination in lead halide perovskite nanocrystals. *Angewandte Chemie* **132**, 14398-14401 (2020).
3. Quintero-Bermudez, R. et al. Small-band-offset perovskite shells increase Auger lifetime in quantum dot solids. *ACS Nano* **11**, 12378-12384 (2017).
4. Zhang, Y. et al. Influence of the surface modification on carrier kinetics and ASE of evaporated perovskite film. *IEEE Photonics Technology Letters* **35**, 285-288 (2023).
5. Zhan, Z. et al. Thermally evaporated MAPbBr₃ perovskite random laser with improved speckle-free laser imaging. *ACS Photonics* **10**, 3077-3086 (2023).
6. Yang, H. et al. Universal surface repairing strategy enabling suppressed Auger recombination in CsPbBr₃ perovskite quantum dots for low threshold lasing in a superlattice microcavity. *Advanced Optical Materials*, 2400141 (2024).
7. Yan, D. et al. Ultrastable CsPbBr₃ perovskite quantum dot and their enhanced amplified spontaneous emission by surface ligand modification. *Small* **15**, 1901173 (2019).
8. Li, J. et al. Simple approach to improving the amplified spontaneous emission properties of perovskite films. *ACS Applied Materials & Interfaces* **8**, 32978-32983 (2016).
9. Pan, J. et al. Air-stable surface-passivated perovskite quantum dots for ultra-robust, single-and two-photon-induced amplified spontaneous emission. *The Journal of Physical Chemistry Letters* **6**, 5027-5033 (2015).
10. Zhang, D. et al. Investigation of random lasing from all-inorganic halide perovskite quantum dots prepared under ambient conditions. *Nanoscale* **13**, 3246-3251 (2021).
11. Qaid, S.M. et al. Fabrication of thin films from powdered cesium lead bromide

(CsPbBr₃) perovskite quantum dots for coherent green light emission. *ACS Omega* **5**, 30111-30122 (2020).

12. Qaid, S.M. et al. Tuning of amplified spontaneous emission wavelength for green and blue light emission through the tunable composition of CsPb(Br_{1-x}Cl_x)₃ inorganic perovskite quantum dots. *The Journal of Physical Chemistry C* **125**, 9441-9452 (2021).

13. Yakunin, S. et al. Low-threshold amplified spontaneous emission and lasing from colloidal nanocrystals of caesium lead halide perovskites. *Nature Communications* **6**, 8056 (2015).